A dynamic model for ionic polymer–metal composite sensors

Zheng Chen, Xiaobo Tan[1], Alexander Will and Christopher Ziel

Smart Microsystems Laboratory, Department of Electrical and Computer Engineering,
Michigan State University, East Lansing, MI 48824, USA

E-mail: chenzhe1@egr.msu.edu and xbtan@msu.edu

Abstract
A dynamic, physics-based model is presented for ionic polymer–metal composite (IPMC) sensors. The model is an infinite-dimensional transfer function relating the short-circuit sensing current to the applied deformation. It is obtained by deriving the exact solution to the governing partial differential equation (PDE) for the sensing dynamics, where the effect of distributed surface resistance is incorporated. The PDE is solved in the Laplace domain, subject to the condition that the charge density at the boundary is proportional to the applied stress. The physical model is expressed in terms of fundamental material parameters and sensor dimensions and is thus scalable. It can be easily reduced to low-order models for real-time conditioning of sensor signals in targeted applications of IPMC sensors. Experimental results are provided to validate the proposed model.

(Some figures in this article are in colour only in the electronic version)

Nomenclature

α_0	charge–stress coupling constant (J C^{-1})
ΔV	volumetric change (m^3 mol^{-1})
κ_e	dielectric permittivity (F m^{-1})
ϕ	electric potential (V)
ρ	charge density (C m^{-3})
σ	induced stress (Pa)
C^+	cation concentration (mol m^{-3})
C^-	anion concentration (mol m^{-3})
D	electric displacement (C m^{-2})
d	ionic diffusivity (m^2 s^{-1})
E	electric field (V m^{-1})
F	Faraday constant (C mol^{-1})
$F(t)$	external force (N)
h	distance from neutral axis to surface (m)
I	moment of inertia (m^4)
i	short-circuit current (A)
i_p	sensing current density (A m^{-1})
i_s	surface current (A)
J	ion flux vector (A m^{-2})
L	free length of IPMC beam (m)

M	bending moment (N m)
p	fluid pressure (Pa)
Q	sensing charge (C)
R	gas constant (J mol^{-1} K^{-1})
r_0	surface resistance per length and width (Ω)
v	free solvent velocity field (m s^{-1})
W	width of IPMC beam (m)
w	tip deflection (m)
Y	Young's modulus (Pa)

1. Introduction

Ionic polymer–metal composites (IPMCs) form an important category of electroactive polymers and have built-in actuation and sensing capabilities [1, 2]. An IPMC sample typically consists of a thin ion-exchange membrane (e.g. Nafion), chemically plated on both surfaces with a noble metal as electrodes [3]. Transport of ions and solvent molecules within an IPMC under an applied voltage leads to bending motions of the IPMC, and hence the actuation effect. IPMC actuators have various promising applications in biomedical devices, bio/micromanipulation and biomimetic robotics [4–10]. On the other hand, a mechanical stimulus on an IPMC causes redistribution of charges and produces a detectable electrical

---

[1] Author to whom any correspondence should be addressed.

signal, suggesting the use of IPMCs as mechanical sensors for force, pressure, displacement or velocity measurement in medical applications, structural health monitoring and robotics [11–15].

Comparing with the extensive work on modeling of IPMC actuators (see, e.g., [16–24]), research on IPMC sensing models has been relatively limited. De Gennes *et al* proposed a static model based on linear irreversible thermodynamics to capture both actuation and sensing mechanisms of IPMCs [25]. Using an analogy to piezoelectric materials, Newbury and Leo presented a geometrically scalable 'grey-box' model for IPMC actuators and sensors [17, 26]. The latter model was further elaborated and verified by Bonomo *et al* [27]. Farinholt and Leo derived the charge sensing response for a cantilevered IPMC beam under a step change in tip displacement [28]. The derivation was based on a linear, one-dimensional partial differential equation governing the internal charge dynamics, which was first developed by Nemat-Nasser and Li for studying the actuation response of IPMCs [18]. A key assumption in [28] is that the initial charge density at the boundary is proportional to the applied step deformation. Farinholt and Leo then obtained an analytical but approximate solution by assuming that the solution is separable as a product of temporal and spatial components.

The contribution of the current paper is an explicit, dynamic, physics-based model for IPMC sensors. The starting point of the model development is the same governing PDE as in [18, 28] that describes the charge redistribution dynamics under electrostatic interactions, ionic diffusion and ionic migration along the thickness direction. But this work extends previous studies significantly in three aspects. First, it incorporates the effect of the distributed surface resistance, which is known to influence the actuation and sensing dynamics [29, 30]. The consideration leads to additional dynamics on IPMC surfaces along the length direction. Second, an exact, analytical solution to the PDE is obtained by converting the original time-domain equation to the Laplace-domain version. Third, instead of limiting to step deformation only, an arbitrary mechanical deformation stimulus is allowed, which is of interest for real applications. For the boundary condition, an assumption analogous to that in [28] is made: the charge distribution at the boundary is proportional to the externally applied stress. The derived short-circuit sensing current is related to the mechanical deformation through an infinite-dimensional transfer function involving hyperbolic and square-root terms. The transfer function model is expressed in terms of fundamental physical parameters and sensor dimensions, and is thus geometrically scalable. It can be further reduced to low-order models in the form of rational transfer functions, which are again scalable.

Experiments have been conducted to validate the proposed dynamic model for an IPMC sensor in a cantilever configuration. Good agreement, both in magnitude and in phase, has been achieved between the measured sensing response and the model prediction for periodic mechanical stimulation from 1 to 20 Hz. The results show that considering the surface resistance leads to more accurate predictions. The geometric scalability of the sensor model has also been confirmed without re-tuning of the identified physical parameters. Experiments for an IPMC sensor under a damped oscillatory deformation and a step deformation have further verified the reduced, low-order model. The influence of the IPMC hydration level on the sensing performance has also been studied.

The salient feature of the proposed model is its combination of the usually incompatible advantages of physics-based models and simple models. As a physical model, its effectiveness in predicting sensing responses in experiments provides valuable insight into the sensing mechanism of IPMCs. On the other hand, the model, as a transfer function, is suitable for analysis and design using the rich set of system-theoretic tools. In particular, the reduced low-order models can be conveniently used to construct compensation circuits or algorithms for real-time conditioning of IPMC sensor signals.

The remainder of the paper is organized as follows. The governing PDE is reviewed in section 2. In section 3 the exact solution and thus the model are derived, with and without considering the surface resistance. Model reduction is discussed in section 4. Experimental validation results are presented in section 5. Finally, concluding remarks are provided in section 6.

2. The governing partial differential equation

The governing PDE for charge distribution in an IPMC was first presented in [18] and then used by Farinholt and Leo [28] for investigating the sensing response. Let $\mathbf{D}$, $\mathbf{E}$, ϕ and ρ denote the electric displacement, the electric field, the electric potential and the charge density, respectively. The following equations hold:

$$\mathbf{E} = \frac{\mathbf{D}}{\kappa_e} = -\nabla\phi, \tag{1}$$

$$\nabla \cdot \mathbf{D} = \rho = F(C^+ - C^-), \tag{2}$$

where κ_e is the effective dielectric constant of the polymer, F is Faraday's constant, and C^+ and C^- are the cation and anion concentrations, respectively. The continuity expression that relates the ion flux vector $\mathbf{J}$ to C^+ is given by

$$\nabla \cdot \mathbf{J} = -\frac{\partial C^+}{\partial t}. \tag{3}$$

Since the thickness of an IPMC is much smaller than its length or width, one can assume that, inside the polymer, $\mathbf{D}$, $\mathbf{E}$ and $\mathbf{J}$ are all restricted to the thickness direction (x direction). This enables one to drop the boldface notation for these variables. The ion flux consists of diffusion, migration and convection terms:

$$J = -d\left(\nabla C^+ + \frac{C^+ F}{RT}\nabla\phi + \frac{C^+ \Delta V}{RT}\nabla p\right) + C^+ v, \tag{4}$$

where d is the ionic diffusivity, R is the gas constant, T is the absolute temperature, p is the fluid pressure, v the free solvent velocity field and ΔV is the volumetric change, which represents how much the polymer volume swells after taking water. From (2), C^+ can be written as
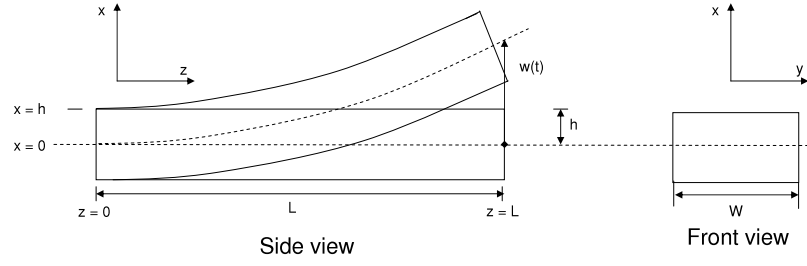
$$C^+ = \frac{1}{F}\rho + C^-, \tag{5}$$

Figure 1. Geometric definitions of an IPMC beam in the cantilevered configuration.

where C^- is homogeneous in space and time-invariant since anions are fixed to the polymer backbone. Taking the gradient with respect to x on both sides of (5) and using (1) and (2), one gets

$$\nabla C^+ = \frac{\kappa_e}{F} \nabla^2 E. \qquad (6)$$

Darcy's Law [31] is used to relate the fluid velocity v to the pressure gradient ∇p [32],

$$v = k'(C^- F E - \nabla p), \qquad (7)$$

where k' denotes the hydraulic permeability coefficient. Neglecting the convection term [28], i.e. assuming $v = 0$, leads to

$$\nabla p = C^- F E. \qquad (8)$$

Substituting (5), (6) and (8) into the original ion flux equation (4) and using $\nabla \phi = -E$, one can rewrite J as

$$J = -d \left(\frac{\kappa_e}{F} \nabla^2 E - \frac{\kappa_e \left(1 - C^- \Delta V \right)}{RT} \nabla E \cdot E \right.$$
$$\left. - \frac{F C^- \left(1 - C^- \Delta V \right)}{RT} E \right). \qquad (9)$$

Assuming $\kappa_e \nabla E \ll C^- F$ (see [19] for justification), the nonlinear term involving $\nabla E \cdot E$ in (9) is dropped, resulting in

$$J = -d \left(\frac{\kappa_e}{F} \nabla^2 E - \frac{F C^-}{RT} \left(1 - C^- \Delta V \right) E \right). \qquad (10)$$

Next writing

$$\frac{\partial C^+}{\partial t} = \frac{1}{F} \frac{\partial \rho}{\partial t} = \frac{\kappa_e}{F} \frac{\partial \left(\nabla E \right)}{\partial t} = \frac{\kappa_e}{F} \frac{\partial^2 E}{\partial x \partial t},$$

and using (3), one obtains the following equation involving E:

$$\frac{\kappa_e}{F} \frac{\partial^2 E}{\partial x \partial t} = d \left(\frac{\kappa_e}{F} \frac{\partial^3 E}{\partial x^3} - \frac{F C^-}{RT} \left(1 - C^- \Delta V \right) \frac{\partial E}{\partial x} \right). \quad (11)$$

Equation (11) can be expressed in terms of $\rho = \kappa_e \nabla E = \kappa_e \frac{\partial E}{\partial x}$:

$$\frac{\partial \rho}{\partial t} - d \frac{\partial^2 \rho}{\partial x^2} + \frac{F^2 d C^-}{\kappa_e RT} \left(1 - C^- \Delta V \right) \rho = 0, \qquad (12)$$

which is the governing PDE for the charge density ρ inside the polymer.

Farinholt and Leo investigated the short-circuit current (and charge) sensing response of a cantilevered IPMC beam when the tip is subject to a step displacement [28], as illustrated in figure 1. Their work is based on obtaining an

analytical but approximate solution $\rho(x, t)$ to (12), which is assumed to take a separable form $\rho(x, t) = P(x) Q(t)$. A key assumption in [28] is that the initial charge density at any point on the IPMC surface along the length direction (denoted as the z direction) is proportional to the induced stress at the same point. This assumption, which serves as an initial/boundary condition for (12), is made based upon that a similar assumption was used in modeling the actuation response of IPMCs [18], and that IPMCs demonstrate reciprocity between sensing and actuation [26]. Note that the solution $\rho(x, t)$ has implicit dependence on the length coordinate z due to the nonuniform stress profile on the surface.

3. Dynamic sensing model

The objective of this paper is to derive a sensing model for IPMCs that accommodate arbitrary mechanical stimuli (including step deformations as a special case). While Farinholt and Leo assume perfectly conducting surface electrodes [28], we also incorporate the distributed surface resistance into the proposed model, which will be shown to produce more accurate predictions in experiments. The model is based upon the exact solution to (12) subject to appropriate boundary conditions, which is made possible by converting it to the Laplace domain. The latter also makes the transfer function a natural representation for the model. Note that only small deflections of the IPMC beam are considered in this paper, where one can ignore the nonlinearity of stress profile as well as the surface resistance variation due to deformation [30].

Consider figure 1, where the beam is clamped at one end ($z = 0$) and is subject to an external force $F(t)$ at the other end ($z = L$) producing the tip displacement $w(t)$. The neutral axis of the beam is denoted by $x = 0$, and the upper and lower surfaces are denoted by $x = h$ and $x = -h$, respectively.

To ease the presentation, define the aggregated constant

$$K \triangleq \frac{F^2 \, dC^-}{\kappa_e RT} \left(1 - C^- \Delta V \right).$$

Performing a Laplace transform for the time variable of $\rho(x, z, t)$, one converts (12) into the Laplace domain:

$$s \rho(x, z, s) - d \frac{\partial^2 \rho(x, z, s)}{\partial x^2} + K \rho(x, z, s) = 0, \qquad (13)$$

where s is the Laplace variable. After rearranging, (13) becomes

$$\frac{\partial^2 \rho(x, z, s)}{\partial x^2} = \frac{(s + K)}{d} \rho(x, z, s). \qquad (14)$$

Define $\beta(s)$ such that $\beta^2(s) = \frac{s+K}{d}$. A generic solution to (14) is obtained as

$$\rho(x, z, s) = c_1(z, s)e^{-\beta(s)x} + c_2(z, s)e^{\beta(s)x}, \quad (15)$$

for some appropriate functions $c_1(z, s)$ and $c_2(z, s)$. An assumption, analogous to the one in [28], will be made to determine $c_1(z, s)$ and $c_2(z, s)$. In particular, it is assumed that the charge density $\rho(\pm h, z, s)$ at the boundary $x = \pm h$ is proportional to the induced stress $\sigma(\pm h, z, s)$:

$$\sigma(\pm h, z, s) = \alpha_0 \rho(\pm h, z, s), \quad (16)$$

where α_0 is the charge–stress coupling constant. From $\sigma(h, z, s) = -\sigma(-h, z, s)$, one gets

$$\rho(h, z, s) + \rho(-h, z, s) = 0,$$

which implies $c_1(z, s) = -c_2(z, s)$ and thus

$$\rho(x, z, s) = 2c_2(z, s)\sinh(\beta(s)x). \quad (17)$$

One can further relate $\sigma(h, s)$ to the external stimuli. In the time domain,

$$\sigma(h, z, t) = \frac{M(z, t)h}{I}, \quad (18)$$

where $M(z, t)$ is the bending moment and $I = \frac{2}{3}Wh^3$ is the moment of inertia, with W being the beam width (refer to figure 1). $M(z, t)$ is related to the external force $F(t)$ at $z = L$ by

$$M(z, t) = F(t)(L - z), \quad (19)$$

where L is the beam length. The out-of-plane deflection $w(t)$ at the tip can be related to the force $F(t)$ by [33]

$$w(t) = \frac{L^3 F(t)}{3YI}, \quad (20)$$

where Y denotes the Young's modulus of the beam. Combining (18)–(20) yields

$$\sigma(h, z, t) = \frac{3Yh(L - z)}{L^3}w(t). \quad (21)$$

Transforming (21) into the Laplace domain and combining with (16), one gets

$$\rho(h, z, s) = \frac{3Yh(L - z)}{\alpha_0 L^3}w(s), \quad (22)$$

which, together with (17), implies

$$c_2(z, s) = \frac{3Yh(L - z)}{2\alpha_0 L^3 \sinh(\beta(s)h)}w(s). \quad (23)$$

Using (17) and the field equations (1) and (2), one can derive the expressions for the electric field E and then for the electric potential ϕ in the Laplace domain:

$$E(x, z, s) = 2c_2(z, s)\frac{\cosh(\beta(s)x)}{\kappa_e\beta(s)} + a_1(z, s), \quad (24)$$

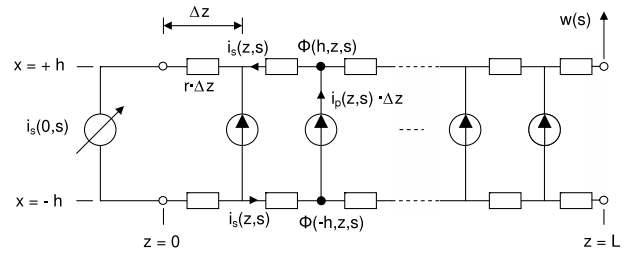$$\phi(x, z, s) = -2c_2(z, s)\frac{\sinh(\beta(s)x)}{\kappa_e\beta^2(s)} - a_1(z, s)x + a_2(z, s), \quad (25)$$

Figure 2. Illustration of the distributed surface resistance for the IPMC sensing model.

where $a_1(z, s)$ and $a_2(z, s)$ are appropriate functions to be determined based on boundary conditions on ϕ. Two different boundary conditions are discussed next, one ignoring the surface electrode resistance and the other considering the resistance. In both cases it will be shown that the final sensing current is proportional to the applied deformation $w(s)$, and thus a transfer function relating the sensor output to the deformation input can be derived.

3.1. Model ignoring the surface resistance

First consider the case where the surface electrodes are perfectly conducting, as was assumed by Farinholt and Leo [28]. In the short-circuit current (or charge) sensing mode, the electric potential is uniform across both surfaces $x = \pm h$, and without loss of generality, the potential is set to be zero:

$$\phi(h, z, s) = \phi(-h, z, s) = 0. \quad (26)$$

Note that the z dependence of ϕ is made explicit in (26) for clarity (but with abuse of notation). Combining (26) with (25), one can solve for $a_1(z, s)$ and $a_2(z, s)$:

$$a_1(z, s) = -2c_2(z, s)\frac{\sinh(\beta((s)h))}{hk_e\beta^2(s)}, \quad (27)$$

$$a_2(z, s) = 0. \quad (28)$$

The total induced sensing charge is obtained by integrating the electrical displacement D on the boundary $x = h$:

$$Q(s) = \int_0^W \int_0^L D(h, z, s)\,dz\,dy = \int_0^W \int_0^L \kappa_e E(h, z, s)\,dz\,dy. \quad (29)$$

Combining (23), (24), (27) and (29), one can derive $Q(s)$ (see the appendix A for details), which is linear with respect to the external stimulus $w(s)$:

$$Q(s) = \frac{3YW(\beta(s)h\coth(\beta(s)h) - 1)}{2\alpha_0 L\beta^2(s)}w(s). \quad (30)$$

The short-circuit current $i(t)$ is the time derivative of the charge $Q(t)$, and hence $i(s) = sQ(s)$ in the Laplace domain. The transfer function from the mechanical input $w(s)$ to the sensing output $i(s)$ is then derived as

$$H_1(s) = \frac{i(s)}{w(s)} = \frac{3sYW(\beta(s)h\coth(\beta(s)h) - 1)}{2\alpha_0 L\beta^2(s)} \quad (31)$$

with $\beta(s) = \sqrt{\frac{s+K}{d}}$.

3.2. Model considering distributed surface resistance

The surface electrode of an IPMC typically consists of aggregated nanoparticles formed during chemical reduction of a noble metal salt (such as platinum salt) [3]. The surface resistance is thus non-negligible and has an influence on the sensing and actuation behaviour of an IPMC [29]. In this paper the effect of distributed surface resistance is incorporated into the sensing model, as illustrated in figure 2. An IPMC beam is clamped at one end ($z = 0$) and is subject to an applied displacement $w(s)$ at the other end ($z = L$). Let the resistance per unit length be $r = r_0/W$, with r_0 representing the surface resistance per unit length and unit width (a parameter independent of IPMC dimensions). For each section Δz of the IPMC, a current $i_p(z, s)\Delta z$ is generated inside the polymer and then joins the surface current $i_s(z, s)$. Note that, by the continuity of current, the current $i_s(z, s)$ on the top surface equals that on the bottom surface but with an opposite direction. The surface current $i_s(0, s)$ collected at $z = 0$, where $\phi(h, 0, s) = \phi(-h, 0, s) = 0$, is the short-circuit sensing current $i(s)$.

The following equations capture the relationships between the surface current $i_s(z, s)$, the sensing current density $i_p(z, s)$ within the polymer and the electric potential $\phi(\pm h, z, s)$ on the surfaces:

$$\frac{\partial \phi(h, z, s)}{\partial z} = r i_s(z, s) = \frac{r_0}{W} i_s(z, s), \qquad (32)$$

$$\frac{\partial \phi(-h, z, s)}{\partial z} = -r i_s(z, s) = -\frac{r_0}{W} i_s(z, s), \qquad (33)$$

$$\frac{\partial i_s(z, s)}{\partial z} = -i_p(z, s). \qquad (34)$$

From the short-circuit condition at $z = 0$, i.e. $\phi(h, 0, s) = \phi(-h, 0, s) = 0$, the boundary conditions for (25) are derived as:

$$\phi(h, z, s) = \int_0^z \frac{r_0}{W} i_s(\tau, s)\, d\tau, \qquad (35)$$

$$\phi(-h, z, s) = -\int_0^z \frac{r_0}{W} i_s(\tau, s)\, d\tau. \qquad (36)$$

Combining (35) and (36) with (25), one can solve for the functions $a_1(z, s)$ and $a_2(z, s)$ in the generic expression for $\phi(x, z, s)$:

$$a_1(z, s) = -\frac{\int_0^z r_0 i_s(\tau, s)\, d\tau}{hW} - 2 c_2(z, s) \frac{\sinh(\beta(s)h)}{h\kappa_e \beta^2(s)}, \quad (37)$$

$$a_2(z, s) = 0. \qquad (38)$$

Next we will eliminate $i_p(z, s)$ in (34) so that the equation involves $i_s(z, s)$ only, which can then be solved for the sensing output $i_s(0, s)$. Note that the generated sensing charge on a Δz section can be expressed as $D(h, z, s)W\Delta z$, i.e.

$$\frac{i_p(z, s)\Delta z}{s} = D(h, z, s)W\Delta z = \kappa_e E(h, z, s)W\Delta z,$$

implying

$$i_p(z, s) = s\kappa_e E(h, z, s)W. \qquad (39)$$

Evaluating $E(h, z, s)$ using (24) with (23) and (37) plugged in for $c_2(z, s)$ and $a_1(z, s)$, respectively, one gets (after simplification):

$$i_p(z, s) = A(s)(L - z) - B(s) \int_0^z i_s(\tau, s)\, d\tau, \qquad (40)$$

where

$$A(s) = \frac{3sYW\, (\beta(s)h \coth(\beta(s)h) - 1)}{\alpha_0 L^3 \beta^2(s)} w(s), \qquad (41)$$

$$B(s) = \frac{s\kappa_e r_0}{h}. \qquad (42)$$

Plugging (40) into (34), one obtains an integro-differential equation for $i_s(z, s)$:

$$\frac{\partial i_s(z, s)}{\partial z} = -A(s)(L - z) + B(s) \int_0^z i_s(\tau, s)\, d\tau. \qquad (43)$$

Equation (43) can be solved analytically through (yet another) Laplace transform, this time for the z variable. For details, refer to the appendix B. In particular, the short-circuit sensing current $i(s) = i_s(0, s)$ is obtained as

$$i(s) = \frac{3sYW\, (\beta(s)h \coth(\beta(s)h) - 1)}{\alpha_0 L^3 \beta^2(s)}$$
$$\times \frac{\left(1 - \cosh(\sqrt{B(s)}L) + \sqrt{B(s)}L \sinh(\sqrt{B(s)}L)\right)}{B(s) \cosh(\sqrt{B(s)}L)} w(s). \qquad (44)$$

The transfer function from the mechanical input $w(s)$ to the sensor output $i(s)$ is then

$$H_2(s) = \frac{i(s)}{w(s)} = \frac{3sYW\, (\beta(s)h \coth(\beta(s)h) - 1)}{\alpha_0 L^3 \beta^2(s)}$$
$$\times \frac{\left(1 - \cosh(\sqrt{B(s)}L) + \sqrt{B(s)}L \sinh(\sqrt{B(s)}L)\right)}{B(s) \cosh(\sqrt{B(s)}L)}, \qquad (45)$$

where $\beta(s) = \sqrt{\frac{s+K}{d}}$ and $B(s)$ is as defined by (42).

Note that the model $H_2(s)$ incorporating surface resistance is consistent with the model $H_1(s)$ ignoring surface resistance. Indeed, $H_2(s)$ degenerates to $H_1(s)$ when the resistance $r_0 \to 0$. To see this, from (31) and (45), one can write

$$H_2(s) = \frac{2}{L^2} \frac{\left(1 - \cosh(\sqrt{B(s)}L) + \sqrt{B(s)}L \sinh(\sqrt{B(s)}L)\right)}{B(s) \cosh(\sqrt{B(s)}L)}$$
$$\times H_1(s).$$

When $r_0 \to 0$, $\sqrt{B(s)} = \sqrt{s\kappa_e r_0/h} \to 0$. From l'Hôpital's rule,

$$\lim_{a \to 0} \frac{1 - \cosh(aL) + aL \sinh(aL)}{a^2 \cosh(aL)} = \frac{L^2}{2}. \qquad (46)$$

Taking $\sqrt{B(s)}$ to be a in (46), one obtains

$$\lim_{r_0 \to 0} H_2(s) = \frac{2}{L^2} \frac{L^2}{2} H_1(s) = H_1(s).$$

Table 1. Physical constants and directly measured parameters.

F	R	T	Y [10]	h	r_0
$96\,487$ C mol^{-1}	8.3143 J mol^{-1} K^{-1}	300 K	5.71×10^8 Pa	$180\ \mu$m	$6.05\ \Omega$

Table 2. Identified parameters through curve-fitting.

d	C^-	κ_e	α_0
3.32×10^{-11} m^2 s^{-1}	1091 mol m^{-3}	1.88×10^{-3} F m^{-1}	104 J C^{-1}

4. Model reduction

An important motivation for deriving a transfer function-type sensing model $H(s)$ is its potential use for real-time feedback control and for sensor signal conditioning. In the case of feedback control, knowing the sensor dynamics is essential to the controller design [34]. For pure sensing applications (such as structural health monitoring), the knowledge of sensor dynamics allows us to correctly reconstruct the original mechanical stimulus $w(s)$ based on the sensor output $i(s)$, either online or offline. This can be done through inversion of the sensor dynamics:

$$w(s) = H_{\text{inv}}(s)i(s), \qquad (47)$$

where $H_{\text{inv}}(s)$ represents the inverse dynamics

$$H_{\text{inv}}(s) = \frac{1}{H(s)}. \qquad (48)$$

For practical implementation of sensor conditioning or feedback control design, the model $H(s)$ needs to be finite-dimensional, i.e. being a finite-order, rational function of s. However, the sensing models derived earlier, $H_1(s)$ and $H_2(s)$ (equations (31) and (45)), are infinite-dimensional since they involve non-rational functions including $\sinh(\cdot)$, $\cosh(\cdot)$, $\sqrt{\cdot}$, etc. A systematic approach to model reduction is to use the Padé approximation [35], where one can approximate $H_1(s)$ or $H_2(s)$ by a finite-dimensional transfer function with any specified order. However, the resulting coefficients for the reduced model can be complex. In the following we discuss a simpler method for reducing the IPMC sensing models by exploiting specific properties of hyperbolic functions and knowledge about the range of physical parameters. The method is less general than the Padé approximation, but it leads to a more compact formula that is valid within the considered frequency range. The discussion will be focused on $H_2(s)$ since it covers $H_1(s)$ as a special case.

For ease of presentation, decompose $H_2(s)$ as

$$H_2(s) = f(s)g(s),$$

with

$$f(s) = \frac{3sYW\,(\beta(s)h\coth(\beta(s)h) - 1)}{\alpha_0\beta^2(s)L^3}, \qquad (49)$$

$$g(s) = \frac{1 - \cosh\left(\sqrt{B(s)}L\right) + \sqrt{B(s)}L\sinh\left(\sqrt{B(s)}L\right)}{B(s)\cosh\left(\sqrt{B(s)}L\right)}. \qquad (50)$$

Based on the physical parameters (see tables 1 and 2 in section 5), the composite constant $\frac{K}{d}$ is of the order of 10^{12}, which implies

$$|\beta(s)| = \left|\frac{s + K}{d}\right| > 10^6,$$

for $s = j\omega$, where ω denotes the angular frequency of any sinusoidal input. Since the thickness h of an IPMC is typically bigger than 1×10^{-4} m, it can be seen that

$$|\beta(s)h| \gg 10,$$

which allows one to make the approximation

$$\coth(\beta(s)h) \approx 1. \qquad (51)$$

With (51), one can simplify (49) as

$$f(s) \approx \frac{3sYW\,(\beta(s)h - 1)}{\alpha_0\beta^2(s)L^3} = \frac{3sYWd}{\alpha_0L^3}\frac{\sqrt{\frac{s+K}{d}}h - 1}{s + K}$$

$$= \frac{3sYW\sqrt{d}\left(\sqrt{s + K}h - \sqrt{d}\right)}{\alpha_0L^3(s + K)}.$$

One can further approximate $\sqrt{s + K}$ by its Taylor series about $s = 0$. For instance, considering up to the second-order terms results in the following approximation to $f(s)$:

$$f(s) \approx \frac{3sYW\sqrt{d}\left(h\sqrt{K}(1 + \frac{s}{2K} - \frac{s^2}{8K^2}) - \sqrt{d}\right)}{\alpha_0L^3(s + K)}. \qquad (52)$$

The following Taylor series expansions of $\sinh(a)$ and $\cosh(a)$ will be used for $g(s)$:

$$\sinh(a) = a + \frac{a^3}{3!} + \frac{a^5}{5!} + \cdots,$$

$$\cosh(a) = 1 + \frac{a^2}{2!} + \frac{a^4}{4!} + \cdots,$$

with $a = \sqrt{B(s)}L$. This results in

$$g(s) = \left[\left(1 - \frac{1}{2!}\right)B(s)L^2 + \left(\frac{1}{3!} - \frac{1}{4!}\right)B^2(s)L^4 \right.$$

$$\left. + \left(\frac{1}{5!} - \frac{1}{6!}\right)B^3(s)L^6 + \cdots\right]$$

$$\times \left[B(s)\left(1 + \frac{B(s)L^2}{2!} + \frac{B^2(s)L^4}{4!} + \cdots\right)\right]^{-1}. \qquad (53)$$

Recall $B(s) = s\kappa_e r_0/h$. Truncation of the series in (53) leads to a finite-order approximation. For example, keeping the first
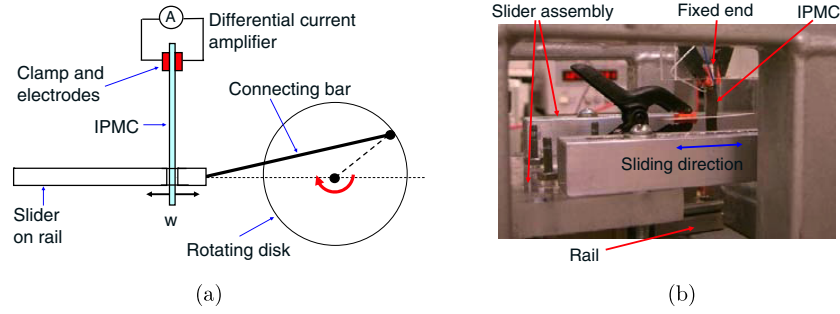
Figure 3. (a) Schematic of the experimental set-up; (b) picture showing a cantilevered IPMC under mechanical deformation.

three terms in each series yields

$$g(s) \approx \left[\left(1 - \frac{1}{2!}\right) B(s)L^2 + \left(\frac{1}{3!} - \frac{1}{4!}\right) B^2(s)L^4 \right.$$
$$\left. + \left(\frac{1}{5!} - \frac{1}{6!}\right) B^3(s)L^6 \right] \left[B(s) \left(1 + \frac{B(s)L^2}{2!} \right. \right.$$
$$\left. \left. + \frac{B^2(s)L^4}{4!}\right) \right]^{-1}. \tag{54}$$

Combining (52) and (53) leads to a fourth-order model for IPMC sensors:

$$\hat{H}(s) = \frac{3sYW\sqrt{d}\left(h\sqrt{K}(1 + \frac{s}{2K} - \frac{s^2}{8K^2}) - \sqrt{d}\right)}{\alpha_0 L^3(s + K)}$$
$$\times \frac{\left(1 - \frac{1}{2!}\right) B(s)L^2 + \left(\frac{1}{3!} - \frac{1}{4!}\right) B^2(s)L^4 + \left(\frac{1}{5!} - \frac{1}{6!}\right) B^3(s)L^6}{B(s)\left(1 + \frac{B(s)L^2}{2!} + \frac{B^2(s)L^4}{4!}\right)}. \tag{55}$$

Although $\hat{H}(s)$ is an improper rational function, i.e. the numerator is of higher order than the denominator, it is not a concern for feedback or sensing applications. This is because the inverse dynamics (48), which is what matters in implementation, will be proper.

Note that a reduced model like (55) is still a physical model. In particular, it is described in terms of fundamental physical parameters and is thus geometrically scalable. This represents a key difference from other low-order, black-box models, in which case the parameters have no physical meanings and one would have to re-identify the parameters empirically for every sensor.

5. Experimental verification

5.1. Experimental set-up

An experimental set-up was built to produce periodic mechanical stimulus with controlled frequency. The schematic of the set-up is shown in figure 3 (a), while figure 3(b) shows its picture. A crank-slider mechanism is used to convert the rotational motion generated by a DC motor (GM8724S009, Pittman) into the linear, oscillatory motion of the slider, which slides on a fixed rail. A rigid bar connects the slider and the rotating disk, and by changing the distance from the bar end to the disk center, the amplitude of translational motion can be adjusted. The oscillation frequency is controlled by tuning the voltage input to the motor, and it is measured through an optical

switch. The set-up can provide periodic excitation from 1 to 20 Hz.

The free end of a cantilevered IPMC beam is constrained to a slit in the slider, which correlates the slider motion directly with the tip-bending deformation $w(t)$ of the IPMC. During operation, the contact point between the IPMC beam and the slider changes slightly. For relatively small oscillation amplitude, the contact point can be treated as fixed, which is close to the beam tip. In all experiments, the oscillation amplitudes were chosen to be 2 mm, which is small compared to the beam length.

A differential current-amplifier circuit is used to measure the IPMC sensing current generated under the mechanical stimulus. Data acquisition and processing are performed through a PC running on a real-time Linux kernel.

5.2. Parameter identification

In the dynamic sensing models $H_1(s)$ and $H_2(s)$, some parameters are physical constants (gas constant R and Faraday's constant F), some can be measured directly (absolute temperature T, Young's modulus Y, sensor dimensions and surface resistance density r_0), and the others need to be identified through curve-fitting. Table 1 lists the physical constants and the parameters obtained through direct measurement. Since $|C^- \Delta V| \ll 1$ [18], we take $1 - C^- \Delta V$ to be 1. The IPMC materials used in this work were obtained from Environmental Robots Inc., and all samples were cut from the same sheet to ensure consistent chemical makeup. Since the IPMC sensing response and thus the model parameters depend on the hydration level and other conditions of the sample, extra care was taken to ensure consistent conditions for all experiments except those in section 5.4. To achieve this, an IPMC sample was soaked in water for several minutes to get fully hydrated, and then mechanically excited in air for ten minutes to get rid of excessive water before each experiment.

The thickness of samples is 360 μm, i.e. $h = 180$ μm. For an IPMC that is 22 mm long and 7 mm wide, the surface resistance was measured to be 19 Ω, corresponding to $r_0 = 6.05$ Ω. The parameters that remain to be determined include the diffusion coefficient d, the anion concentration C^-, the dielectric constant κ_e and the charge–stress coupling constant α_0. The empirical frequency response of an IPMC sensor with dimensions 22×7 mm was used to identify the remaining parameters through a nonlinear curve-fitting process, as described next.
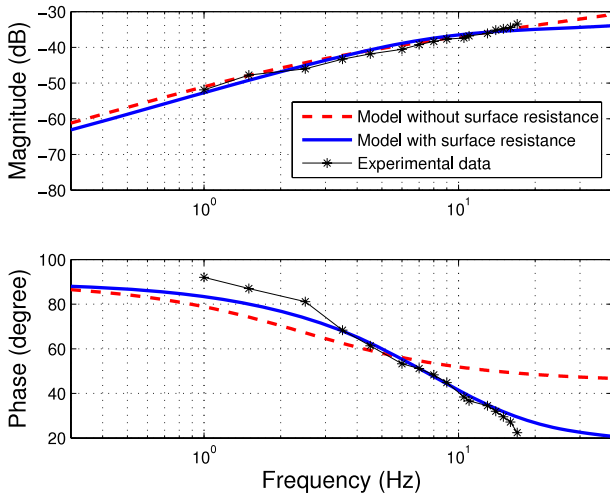
Figure 4. Performance of the models with and without consideration of surface resistance.

Figure 5. Frequency responses of the sensing dynamics for the *big* and *slim* samples.

Fix an excitation frequency f and acquire the mechanical deformation $w(t)$ and the IPMC sensor output $i(t)$. Fast Fourier transforms are then performed on $w(t)$ and $i(t)$ to extract their amplitudes and phases, based on which one can compute the magnitude gain and the phase shift of the sensor dynamics (from the mechanical input to the sensing output) at that particular frequency. Repeat this process for other excitation frequencies that are available from the experimental set-up (1–20 Hz), which produces the empirical Bode plots for the frequency response.

One can then tune the unknown parameters of the sensor model $H_2(s)$ to fit the empirical frequency response. In particular, $H_2(j2\pi f)$ predicts the magnitude and phase response of the sensor at frequency f, and it is a nonlinear function of the parameters. The Matlab function *fminsearch* can be used to find the parameters that minimize the squared error between the empirical frequency response and the model prediction. The identified parameters are listed in table 2, which are close to the values reported in the literature [18, 28]. For independent verification of the proposed model, the identified parameters will be used in predicting behavior of other IPMC sensors with different dimensions, as will be seen in section 5.3.

5.3. Model verification

Model verification will be conducted on three aspects. First, it will be shown that the model considering the surface resistance is more accurate than the model ignoring the resistance, by comparing them with the measured frequency response of an IPMC sensor. Second, the geometric scalability of the proposed model will be confirmed by the agreement between model predictions and experimental results for IPMC sensors with different dimensions. Third, the performance of the reduced model will be illustrated through its prediction of the time-domain sensing responses under a damped, oscillatory excitation and a step deformation, respectively.

5.3.1. Effect of surface resistance. In order to examine the difference between the models $H_1(s)$ and $H_2(s)$, their model
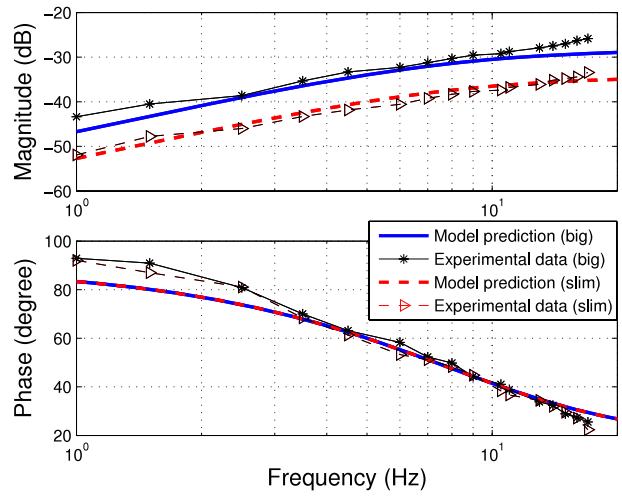
Table 3. Dimensions of three IPMC samples used for verification of model scalability.

IPMC beam	Length (mm)	Width (mm)	Thickness (μm)
Big	22	14	360
Slim	22	7	360
Short	11	7	360

parameters were identified separately through the nonlinear fitting process described in section 5.2. The experimental data were obtained for an IPMC sensor with dimensions $22 \times 7 \times 0.36$ mm. Figure 4 compares the predicted frequency response (both magnitude and phase) by each model with the measured frequency response. Both models show good agreement with the experimental data on the magnitude plot. On the phase plot, however, it is clear that the model considering the surface resistance shows better agreement than the one ignoring the resistance. This indicates that the model incorporating the surface resistance is more effective in capturing the sensing dynamics of IPMC, and thus it will be used for the remainder of this paper.

5.3.2. Geometric scalability of the dynamic model. Three samples with different dimensions (see table 3) were cut from one IPMC sheet and were labeled as *big*, *slim* and *short* for ease of referencing. The length in table 3 represents the free bending length of the IPMC beam. Model parameters were first identified for the *slim* sample, as discussed in section 5.2. Without re-tuning, these parameters (except geometric dimensions) were plugged into (45), i.e. the model $H_2(s)$, for predicting the frequency response for the *big* and *short* samples.

Figure 5 shows the Bode plots of the frequency responses for the *slim* and *big* samples. It can be seen that, for both samples, good agreement between the model prediction and the experimental data is achieved. Furthermore, since the two samples differ only in width, the model (45) predicts that their magnitude responses will differ by $20 \log 2 = 6$ dB uniformly in frequency, while their phase responses will be
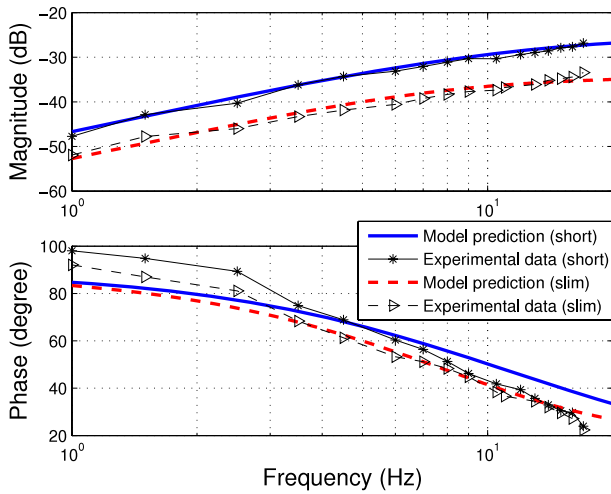
Figure 6. Frequency responses of the sensing dynamics for the *slim* and *short* Samples.

the same. Both predictions are confirmed in the figure: the experimentally measured magnitude responses are parallel to each other with a difference about 6 dB, and the measured phase responses overlap well.

Figure 6 compares the frequency responses of the *slim* and *short* samples. A reasonable match between the model

predictions and the empirical curves is again achieved for both samples. The figure also indicates the need to incorporate the surface resistance in modeling. Since the two samples differ only in length, the model ignoring the surface resistance (equation (31)) will predict that the magnitude responses of the two samples would differ just by a constant while their phase responses would be identical. But the empirical magnitude curve for the *slim* sample increases with frequency by approximately 14 dB per decade, while that for the *short* sample increases by roughly 18 dB per decade. Moreover, the empirical phase curves clearly do not overlap. All these subtle trends, however, are captured well by the model considering the surface resistance, as can be seen in figure 6.

5.3.3. Verification of the reduced model. Experiments were further conducted to verify the effectiveness of the model reduction approach presented in section 4. Two mechanical stimuli, which were different from periodic signals, were used to demonstrate the wide applicability of the proposed model. In the first experiment the cantilevered *slim* IPMC sample was allowed to freely vibrate upon an initial perturbation on the tip. In the second experiment the tip of the cantilevered *big* sample was subject to a step displacement and then held there. A laser displacement sensor (OADM 20I6441/S14F, Baumer Electric) was used to record the tip displacement trajectory $w(t)$. The inverse of fourth-order reduced model (55) was adopted to
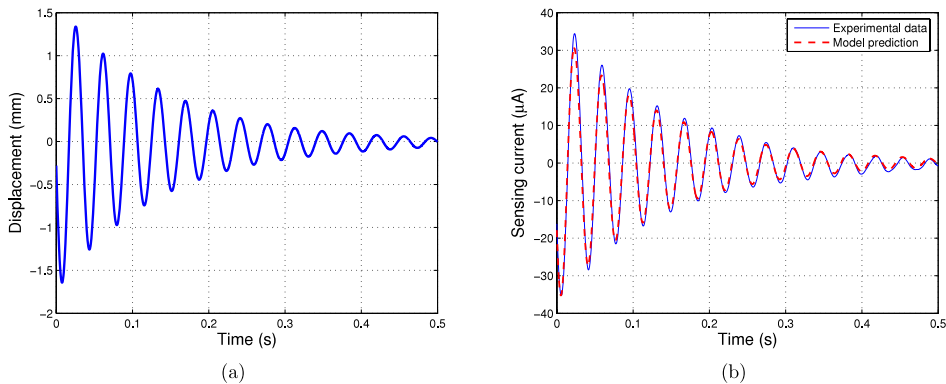

Figure 7. The sensing response of the *slim* sample under a decaying, oscillatory mechanical stimulus. (a) The tip displacement trajectory; (b) prediction of the sensing response versus experimental measurement.
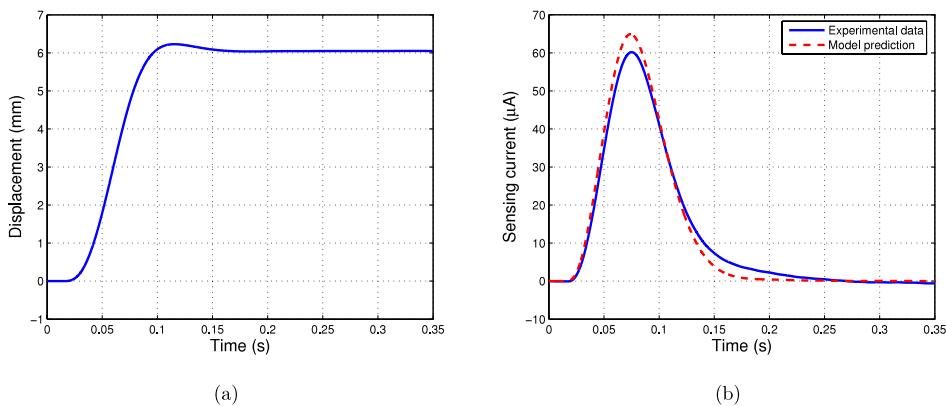

Figure 8. The sensing response of the *big* sample under a step stimulus. (a) The tip displacement trajectory; (b) prediction of the sensing response versus experimental measurement.
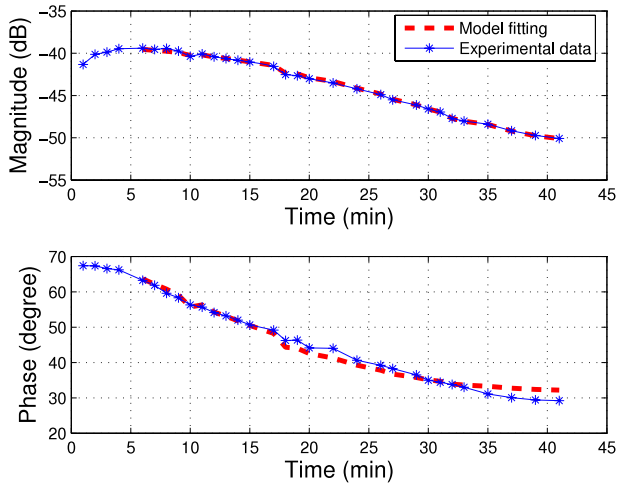
1485

Figure 9. The sensing response at 6 Hz for the *slim* IPMC sample over time.

Figure 10. Identified diffusion coefficient versus time.

predict the bending displacement based on the short-circuit sensing current measurement for each case, where the model parameters from the identification experiment in section 5.2 were used directly.

Figure 7 compares the predicted bending displacement with the experimental measurement under the damped, oscillatory stimulus. The beam has a natural frequency of about 30 Hz, which is outside the frequency range of the signals used in parameter identification, yet the reduced model is able to predict the bending displacement well. Figure 8 shows the model prediction of the bending displacement against the experimental data for the case of a step tip deformation. It can be seen that satisfactory agreement between the predicted and the measured curves is again achieved.

5.4. Impact of hydration level on sensing response

Finally, the proposed dynamic model is explored to gain insight into the dependence of IPMC sensing response on the hydration level of the sample. Such dependence is clearly seen from the experimental curve in figure 9. In this experiment the *slim* IPMC sample was first soaked in water, and then subject to continuous, 6 Hz periodic mechanical excitation in air. Data (both the stimulus and the sensor output) were collected for about 40 min. The frequency response of the sensor at 6 Hz at each minute was then extracted from the data, including the magnitude gain and the phase shift. The evolution of this response is plotted in figure 9 (note that the horizontal axis represents time instead of frequency). The sensing response right after the IPMC was taken out of water was not strong, and it was not steady due to the excessive water inside. This is consistent with what Bonomo *et al* reported in [27]. But we also observed that the amplitude of the sensing signal increased to the maximum at about $t = 5$ min, and it started to decrease afterwards. Bonomo *et al* [27] mentioned that the IPMC still had good sensing response after hours of work, but they did not report quantitatively the evolution history of the sensing signal amplitude.
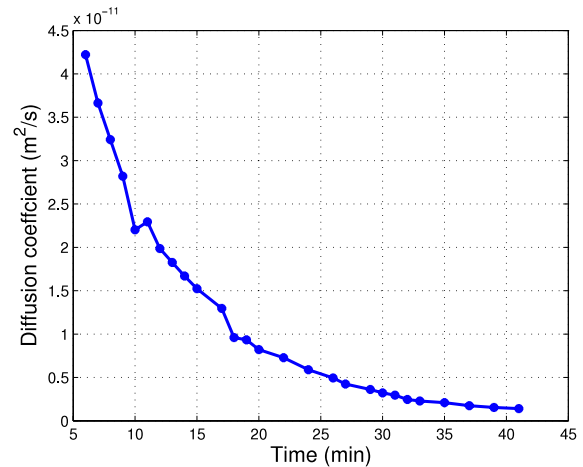
The time-varying response is believed to arise from water evaporation of the IPMC sample. In order to correlate this phenomenon with the proposed model (45), we assume that all parameters except the diffusion coefficient d are constant. Since the sensing signal before $t = 5$ min is noisy and irregular, we have used only the data after $t = 5$ min to identify the diffusion coefficient of the model. Taking the values identified in section 5.2 for those fixed parameters, we identify the evolving value of d by fitting the measured magnitude and phase response at each minute. The dashed curves in figure 9 show the results of model fitting with a time-dependent d. The time trajectory of the identified d is plotted in figure 10 and its decaying trend is consistent with the decreasing hydration level.

Water evaporation could lead to changes in other parameters as well. For instance, the Young's modulus gets bigger as the beam dries up. From the model (45), larger Young's modulus enhances the amplitude of the sensing response and has no effect on the phase response. However, figure 9 shows that, during the experiment, the amplitude response deteriorates while the phase response also varies. This appears to support that the change of Young's modulus is not a dominant factor for the change of sensing response.

The discussions above suggest that the hydration level impacts the sensing behavior of an IPMC through its influence on the ion diffusivity. However, since d cannot be measured directly to confirm the identified trajectory in figure 10, more research is needed before a conclusive statement can be made.

6. Conclusions and discussion

In this paper a dynamic model for IPMC sensors has been developed by solving the physics-governing PDE analytically in the Laplace domain. The model accommodates the surface electrode resistance in an integrative manner. The mechanical stimulus enters as a boundary condition for the PDE and the sensing output is related to the mechanical input linearly. This leads to a compact, explicit, transfer-function representation of the physics-based model, which can be further reduced to low-order models for real-time sensing and feedback control purposes. A number of experimental results were presented

to demonstrate the geometric scalability of the model, as well as its applicability to arbitrary mechanical inputs. Due to the physical nature of the model, the agreement between model predictions and experimental results also provides insight into the underlying sensing mechanisms of IPMC materials.

Note that there are two factors that have enabled us to solve the governing PDE exactly. First, the core equation (12) involves only the thickness coordinate x and is thus one-dimensional. This is appropriate since the length and the width of an IPMC are much larger than its thickness, making the sample appear like a parallel-plate transmission line. Second, the PDE is linear, after a nonlinear term is discarded during the derivation (see section 2). The latter is justified by the generally satisfactory performance of the derived model. On the other hand, some of the discrepancies between the model predictions and the experimental measurement could be due to the unmodeled nonlinearity, which is a subject of ongoing study.

The proposed modeling approach can be extended in several directions. The mechanical input used in this paper has been the IPMC tip displacement, since it was directly controlled and measured in our experimental set-up. One can easily switch to other mechanical inputs (e.g. velocity or force). It is also possible to consider other IPMC configurations, such as a double-clamped beam or an IPMC plate. Finally, a similar approach can be taken to model the actuation behavior of IPMCs.

Acknowledgments

Appendix A. Derivation of equation (30)

From (29), one gets

$$
\begin{aligned}
Q(s) &= \int_0^W \int_0^L \kappa_e \Big[2c_2(z,s) \frac{\cosh(\beta(s)h)}{\kappa_e \beta(s)} \\
&\quad - 2c_2(z,s) \frac{\sinh(\beta(s)h)}{h\kappa_e \beta^2(s)} \Big] dz\, dy \\
&= \frac{2W\,(\beta(s)h\cosh(\beta(s)h) - \sinh(\beta(s)h))}{h\beta^2(s)} \int_0^L c_2(z,s)\,dz \\
&= \frac{2W\,(\beta(s)h\cosh(\beta(s)h) - \sinh(\beta(s)h))}{h\beta^2(s)} \\
&\quad \times \int_0^L \frac{3Yh(L-z)w(s)}{2\alpha_0 L^3 \sinh(\beta(s)h)}\,dz \\
&= \frac{3YW\,(\beta(s)h\coth(\beta(s)h) - 1)\,w(s)}{\alpha_0 L^3 \beta^2(s)} \int_0^L (L-z)\,dz \\
&= \frac{3YW\,(\beta(s)h\coth(\beta(s)h) - 1)}{2\alpha_0 L\beta^2(s)} w(s),
\end{aligned}
$$

which is (30). In the above the first equality is from (24) and (27), the second equality follows from the independence of $c_2(z,s)$ from y, and the third equality is from (23).

Appendix B. Solving the integro-differential equation (43)

We introduce the unilateral Laplace transform for functions of the length coordinate z. The new Laplace variable will be denoted as p since s has already been used for the transform of time functions. For instance, the transform of $i_s(z,s)$ will be defined as

$$
I_s(p,s) \triangleq \int_0^\infty i_s(z,s)e^{-pz}\,dz.
$$

Now perform the Laplace transform with respect to the z variable on both sides of (43). Using properties of Laplace transforms [34, 36], one gets

$$
pI_s(p,s) - i_s(0,s) = -A(s)\left(\frac{L}{p} - \frac{1}{p^2}\right) + B(s)\frac{I_s(p,s)}{p}. \tag{B.1}
$$

Solving for $I_s(p,s)$, one obtains

$$
I_s(p,s) = \frac{p}{p^2 - B(s)} i_s(0,s) - \frac{pL - 1}{p\left(p^2 - B(s)\right)} A(s), \tag{B.2}
$$

which can be rewritten through partial fraction expansion as:

$$
\begin{aligned}
I_s(p,s) &= \frac{1}{2}\left(\frac{1}{p - \sqrt{B(s)}} + \frac{1}{p + \sqrt{B(s)}}\right) i_s(0,s) \\
&\quad + \left(\frac{q_1(s)}{p} + \frac{q_2(s)}{p - \sqrt{B(s)}} + \frac{q_3(s)}{p + \sqrt{B(s)}}\right) A(s), \tag{B.3}
\end{aligned}
$$

with

$$
q_1(s) = -\frac{1}{B(s)}, \qquad q_2(s) = \frac{1 - L\sqrt{B(s)}}{2B(s)},
$$
$$
q_3(s) = \frac{1 + L\sqrt{B(s)}}{2B(s)}.
$$

The surface current $i_s(z,s)$ is then obtained from (B.3) using the inverse Laplace transform of $I_s(p,s)$:

$$
\begin{aligned}
i_s(z,s) &= \frac{e^{\sqrt{B(s)}z} + e^{-\sqrt{B(s)}z}}{2} i_s(0,s) \\
&\quad + \left(-\frac{1}{B(s)} + \frac{1 - \sqrt{B(s)}L}{2B(s)} e^{\sqrt{B(s)}z}\right. \\
&\quad \left. + \frac{1 + \sqrt{B(s)}L}{2B(s)} e^{-\sqrt{B(s)}z}\right) A(s) \\
&= \cosh(\sqrt{B(s)}z) i_s(0,s) + \Big(-1 + \cosh(\sqrt{B(s)}z) \\
&\quad - \sqrt{B(s)}L \sinh(\sqrt{B(s)}z)\Big)\frac{A(s)}{B(s)}. \tag{B.4}
\end{aligned}
$$

Refer to figure 2. Since the circuit is open at $z = L$, the following holds:

$$
i_s(L,s) = 0. \tag{B.5}
$$

Plugging $z = L$ into (B.4) and using (B.5), one obtains the sensing current $i_s(0,s)$ as

$$
i_s(0,s) = \frac{A(s)(1 - \cosh(\sqrt{B(s)}L) + \sqrt{B(s)}L\sinh(\sqrt{B(s)}L))}{B(s)\cosh(\sqrt{B(s)}L)}. \tag{B.6}
$$

References

[1] Shahinpoor M and Kim K 2001 Ionic polymer–metal composites: I. Fundamentals *Smart Mater. Struct.* **10** 819–33

[2] Bar-Cohen Y 2004 Electric flex *IEEE Spectrum* **41** 29–33

[3] Kim K J and Shahinpoor M 2003 Ionic polymer-metal composites: II. Manufacturing techniques *Smart Mater. Struct.* **12** 65–79

[4] Tadokoro S, Yamagami S and Ozawa M 1999 Soft micromanipulation device with multiple degrees of freedom consisting of high polymer gel actuators *Proc. IEEE Int. Conf. on Micro Electro Mechanical Systems* pp 37–42

[5] Guo S, Fukuda T and Asaka K 2003 A new type of fish-like underwater microrobot *IEEE/ASME Trans. Mechatronics* **8** 136–41

[6] Kim B, Ryu J, Jeong Y, Tak Y, Kim B and Park J-O 2003 A ciliary based 8-legged walking micro robot using cast IPMC actuators *Proc. IEEE Int. Conf. on Robots and Automation* pp 2940–5

[7] Shahinpoor M and Kim K 2005 Ionic polymer-metal composites: IV. Industrial and medical applications *Smart Mater. Struct.* **14** 197–214

[8] Yamakita M, Kamamichi N, Kozuki T, Asaka K and Luo Z 2005 Control of biped walking robot with IPMC linear actuator *Proc. IEEE/ASME Int. Conf. on Advanced Intelligent Mechatronics (Monterey, CA, 2005)* pp 48–53

[9] Tan X, Kim D, Usher N, Laboy D, Jackson J, Kapetanovic A, Rapai J, Sabadus B and Zhou X 2006 An autonomous robotic fish for mobile sensing *Proc. IEEE/RSJ Int. Conf. on Intelligent Robots and Systems (Beijing, 2006)* pp 5424–9

[10] Chen Z, Shen Y, Xi N and Tan X 2007 Integrated sensing for ionic polymer-metal composite actuators using PVDF thin films *Smart Mater. Struct.* **16** S262–71

[11] Mojarrad M and Shahinpoor M 1997 Ion-exchange–metal composite sensor films *Smart Structures and Materials 1997: Smart Sensing, Processing, and Instrumentation*; *Proc. SPIE* **3042** 52–60

[12] Ferrara L, Shahinpoor M, Kim K J, Schreyer H B, Keshavarzi A, Benzel E and Lantz J W 1999 Use of ionic polymer-metal composites (IPMCs) as a pressure transducer in the human spine *Smart Structures and Materials 1999: Electroactive Polymer Actuators and Devices*; *Proc. SPIE* **3669** 394–401

[13] Keshavarzi A, Shahinpoor M, Kim K J and Lantz J W 1999 Blood pressure, pulse rate, and rhythm measurement using ionic polymer-metal composite sensors *Smart Structures and Materials 1999: Electroactive Polymer Actuators and Devices*; *Proc. SPIE* **3669** 369–76

[14] Konyo M, Konishi Y, Tadokoro S and Kishima T 2004 Development of velocity sensor using ionic polymer-metal composites *Smart Structures and Materials 2004: Electroactive Polymer Actuators and Devices*; *Proc. SPIE* **5385** 307–18

[15] Bonomo C, Fortuna L, Giannone P and Graziani S 2004 A sensor–actuator integrated system based on IPMCs *Proc. IEEE Sensors* pp 489–92

[16] Kanno R, Tadokoro S, Takamori T and Hattori M 1996 Linear approximate dynamic model of IPMC (ionic conducting polymer gel film) actuator *Proc. IEEE Int. Conf. on Robotics and Automation (Minneapolis, MN, 1996)* pp 219–25

[17] Newbury K 2002 Characterization, modeling, and control of ionic polymer transducers *PhD Thesis* Virginia Polytechnic Institute and State University, Blacksburg, Virgina

[18] Nemat-Nasser S and Li J 2000 Electromechanical response of ionic polymer-metal composites *J. Appl. Phys.* **87** 3321–31

[19] Nemat-Nasser S 2002 Micromechanics of actuation of ionic polymer-metal composites *J. Appl. Phys.* **92** 2899–915

[20] Tadokoro S, Fukuhara M, Maeba Y, Konyo M, Takamori T and Oguro K 2002 A dynamic model of ICPF actuator considering ion-induced lateral strain for molluskan robotics *Proc. IEEE/RSJ Int. Conf. on Intelligent Robots and Systems (Lausanne, Switzerland, 2002)* pp 2010–7

[21] Shahinpoor M and Kim K J 2004 Ionic polymer-metal composites: III. Modeling and simulation as biomimetic sensors, actuators, transducers, and artificial muscles *Smart Mater. Struct.* **13** 1362–88

[22] Chen Z, Tan X and Shahinpoor M 2005 Quasi-static positioning of ionic polymer-metal composite (IPMC) actuators *Proc. IEEE/ASME Int. Conf. on Advanced Intelligent Mechatronics (Monterey, CA, 2005)* pp 60–5

[23] Costa Branco P J and Dente J A 2006 Derivation of a continuum model and its electric equivalent-circuit representation for ionic polymer-metal composite (IPMC) electromechanics *Smart Mater. Struct.* **15** 378–92

[24] Bonomo C, Fortuna L, Giannone P, Graziani S and Strazzeri S 2007 A nonlinear model for ionic polymer metal composites as actuators *Smart Mater. Struct.* **16** 1–12

[25] de Gennes P G, Okumura K, Shahinpoor M and Kim K 2000 Mechanoelectric effects in ionic gels *Europhys. Lett.* **50** 513–8

[26] Newbury K M and Leo D J 2002 Electromechanical modeling and characterization of ionic polymer benders *J. Intell. Mater. Syst. Struct.* **13** 51–60

[27] Bonomo C, Fortuna L, Giannone P, Graziani S and Strazzeri S 2006 A model for ionic polymer metal composites as sensors *Smart Mater. Struct.* **15** 749–58

[28] Farinholt K and Leo D 2004 Modeling of electromechanical charge sensing in ionic polymer transducers *Mech. Mater.* **36** 421–33

[29] Shahinpoor M and Kim K J 2000 The effect of surface-electrode resistance on the performance of ionic polymer-metal composite (IPMC) artificial muscles *Smart Mater. Struct.* **9** 543–51

[30] Punning A, Kruusmaa M and Aabloo A 2007 Surface resistance experiments with IPMC sensors and actuators *Sensors Actuators* A **133** 200–9

[31] Darcy H 1856 *Les Fontaines Publiques de la Ville de Dijon* (Paris: Dalmont)

[32] Grimshaw P, Nussbaum J and Grodzinsky A 1990 Kinetics of electrically and chemically induced swelling in polyelectrolyte gels *J. Chem. Phys.* **93** 4462–72

[33] Popov E 1976 *Mechanics of Materials* 2nd edn (Englewood Cliffs, NJ: Prentice-Hall)

[34] Franklin G F, Powell J D and Emami-Naeini A 2006 *Feedback Control of Dynamic Systems* 5th edn (Upper Saddle River, NJ: Pearson Education)

[35] Baker G A and Graves-Morris P 1996 *Padé Approximants* (New York: Cambridge University Press)

[36] Churchill R V 1972 *Operational Mathematics* 3rd edn (New York: McGraw-Hill)